

Learning to Fit Morphable Models

Vasileios Choutas^{1*} Federica Bogo² Jingjing Shen² Julien Valentin²

¹Max Planck Institute for Intelligent Systems, Tübingen, Germany ²Microsoft

vchoutas@tue.mpg.de {febogo, jinshen, valentin.julien} @ microsoft.com

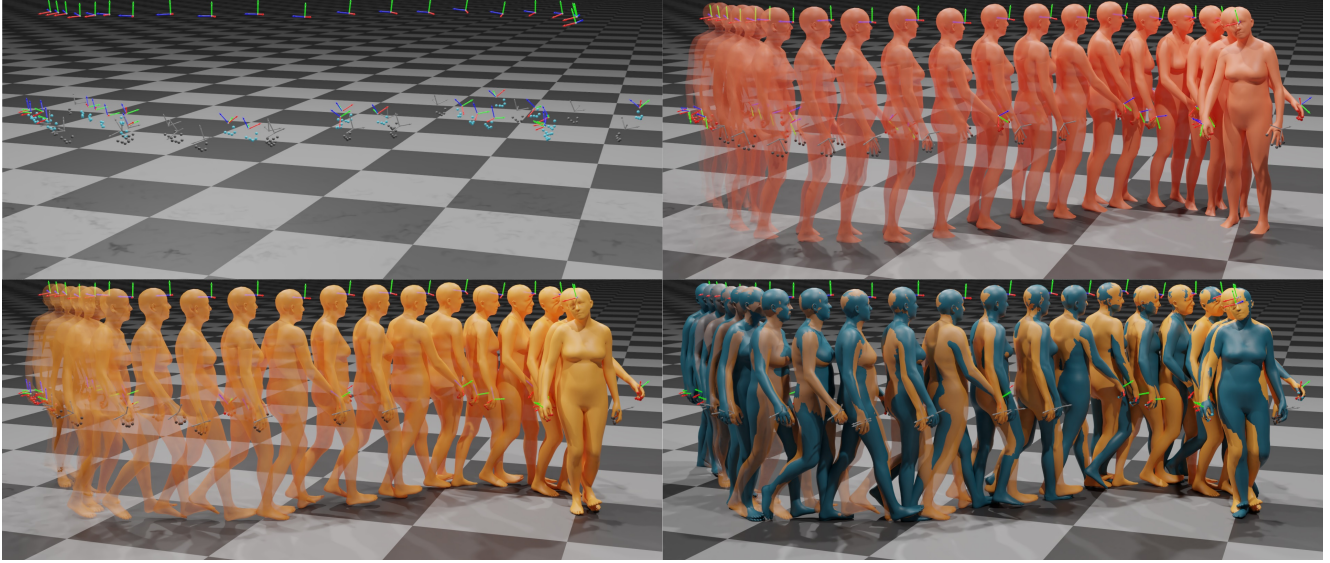


Figure 1. Accurate head and hand poses are becoming readily available on AR and VR headsets. One current challenge to increase immersion in virtual worlds consists in fitting 3D body models to these sparse measurements (top left) which is a problem often tackled using regression followed by iterative mathematical optimization (top right). While these approaches have demonstrated their effectiveness on many problems, they require significant amounts of manual labor to work at speed and quality. Using machine learning for continuous optimization offers the opportunity to overcome this hurdle by learning the priors directly from the data and by leveraging optimized back-end implementations (bottom left). In this way, we can construct effective models, without the biases introduced by the manually defined energy terms. The resulting models are fast, able to tightly fit the data (bottom right, ground-truth mesh in blue) and can easily be trained for different problem setups. Note that all results are estimated independently per-frame.

Abstract

Fitting parametric models of human bodies, hands or faces to sparse input signals in an accurate, robust, and fast manner has the promise of significantly improving immersion in AR and VR scenarios. A common first step in systems that tackle these problems is to regress the parameters of the parametric model directly from the input data. This approach is fast, robust, and is a good starting point for an iterative minimization algorithm. The latter searches for the minimum of an energy function, typically composed of a data term and priors that encode our knowledge about the problem’s structure. While this is undoubtedly a very successful recipe, priors are often hand defined heuristics and finding the right balance between the

different terms to achieve high quality results is a non-trivial task. Furthermore, converting and optimizing these systems to run in a performant way requires custom implementations that demand significant time investments from both engineers and domain experts. In this work, we build upon recent advances in learned optimization and propose an update rule inspired by the classic Levenberg–Marquardt algorithm. We show the effectiveness of the proposed neural optimizer on the problems of 3D body surface estimation from a head-mounted device and face fitting from 2D landmarks. Our method can easily be applied to new model fitting problems and offers a competitive alternative to well-tuned ‘traditional’ model fitting pipelines, both in terms of accuracy and speed.

* Work performed during an internship at Microsoft.

1. Introduction

Fitting parametric models [16, 29, 51, 53, 69] to noisy input data is one of the most common tasks in computer vision. Notable examples include parametric model fitting of bodies [7, 12, 18, 33, 36, 51, 67], faces [16], and hands [4, 8, 23, 58].

Direct regression using neural networks is the de facto default tool to estimate model parameters from observations. While the obtained predictions are robust and accurate to large extent, they often fail to tightly fit the observations [76] and require large quantities of annotated data. Classic optimization methods, e.g. the Levenberg-Marquardt algorithm [38, 44] can tightly fit the parametric model to the data by iteratively minimizing a hand-crafted energy function but are prone to local minimas and can require many iterations to converge when seeded far from the solution. Hence, practitioners often combine these two approaches by first initializing the model parameters from a regressor followed by a few steps of energy minimization using a classic optimizer, effectively allowing to combine the benefits of both approaches.

If we look one level deeper, optimization based model fitting methods have another disadvantage of often requiring hand-crafted energy functions that are difficult to define and non-trivial to tune. Each fitting problem effectively requires the definition of different data terms, prior terms and regularization terms. Besides the work required to formulate the different parts of the energy and possibly train the priors, domain experts needs to spend significant amounts of time to balance the effect of each term. Since these priors are often hand-defined or assumed to follow distributions that are tractable / easy to optimize, the resulting fitting energy usually contains biases that can limit the accuracy of the resulting fits.

To get the best of both regression using deep learning and classical numerical optimization, we propose to turn to the field of machine learning based continuous optimization. Here, instead of updating the model parameters using a first or second order model fitter, a network learns to iteratively update the parameters that minimize the target loss. By training the network end-to-end, we can directly leverage optimized ML back-ends and avoid the need for hand-crafted priors since the network can directly learn the subspace of valid model parameters from data.

Our main contribution is an iterative machine learning solver which uses a learnt update rule inspired from the Levenberg-Marquardt algorithm. Instead of using raw network outputs to update the model parameters, we propose to combine the gradient descent direction and the update predicted from a GRU. We evaluate our approach on different challenging scenarios namely full-body tracking from head and hand inputs only and face tracking from 2D landmarks, demonstrating both high quality results and versatility of the

proposed framework to different model fitting tasks.

2. Related work

Learning to optimize [2, 55, 56] is a field that casts optimization as a learning problem. The goal is to create models that learn to exploit the problem structure, producing faster and more effective energy minimizers. In this way, we can remove the need for hand-designed parameter update rules and priors, since we can learn them directly from the data. This approach has been used for image denoising and depth-from-stereo estimation [64], rigid motion estimation [41], view synthesis [19], non-linear tomographic inversion problem with simulated data [1] and object reconstruction from a single image [35].

Parametric human model fitting: The seminal work of Blanz and Vetter [6] introduced a parametric model of human faces and a user-assisted method to fit the model to images. Since then, the field has evolved and produced better face models and faster, more accurate and more robust estimation methods [16]. With the introduction of SMPL [40], the field of 3D body pose and shape estimation has been rapidly progressing. The community has created large motion databases [42] from motion capture data, as well as datasets, both real and synthetic, with images and corresponding 3D bodies [22, 50, 65]. Thanks to these, we can now train neural network regressors that can reliably predict SMPL parameters from images [28, 36, 37, 39, 76] and videos [11, 32]. With the introduction of expressive models [29, 51, 69], the latest regression approaches [12, 18, 54] can now predict the 3D body, face and hands. However, one common issue, present in all regression scenarios, is the misalignment of the predictions and the input data [57, 76]. Thus, they often serve as the initial point for an optimization-based method [7, 51, 67], which refines the estimated parameters until some convergence criterion is met. This combination produces system that are effective, robust and able to work in real-time and under challenging conditions [45, 58, 61]. However, formulating the correct energy terms and finding the right balance between them is a challenging and time-consuming task. Furthermore, adapting the optimizer to run in real-time is a non-trivial operation, due to the cubic complexity of the popular Levenberg-Marquardt algorithm [26, 38, 44]. The most common and practical way to speedup the optimization is to utilize the sparsity of the problem or make certain assumptions to simplify it [17]. Learned optimizers promise to overcome these issues, by learning the parametric model priors directly from the data and to take more aggressive steps, thus converging in fewer iterations. The effectiveness of these approaches has been demonstrated in different scenarios, such as fitting a body model [40, 69] to images [59, 75] and videos [73], to sparse sensor data from electromagnetic sensors [30] and multi-body estimation from

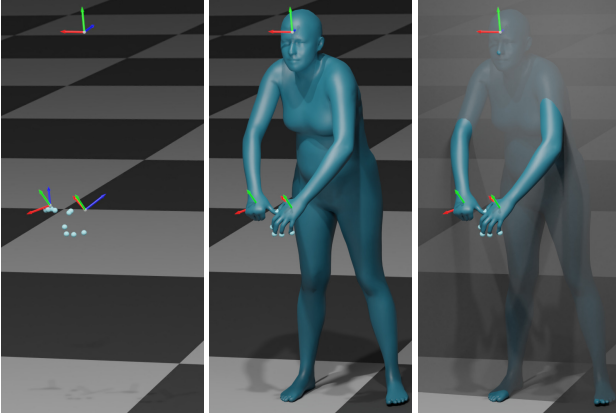


Figure 2. The left shows the input 6-DoF transformations $T_H, T_L, T_R \in SE(3)$ and fingertip positions $P_{i=1,\dots,5}^L, P_{i=1,\dots,5}^R$ returned by the head-mounted device. The middle shows the corresponding ground-truth mesh, obtained by MoSh'ing [42] MoCap markers. The right illustrates the half-space visibility scenario, where everything behind the plane formed by the up and right vectors of the headset is considered not observed.

multi-view images [15]. We propose an update rule, applicable to all of the above scenarios, that is inspired from classic methods and shows superior performance compared to using a pure network update.

Estimating 3D human pose from a head-mounted device is a difficult problem, due to self-occlusions caused by the position of the headset and the sparsity of the input signals [70]. Yuan and Kitani [71, 72] cast this as a control problem, where a model learns to produce target joint angles for a Proportional-Derivative (PD) controller. Other methods [62, 63] tackle this as a learning problem, where a neural network learns to predict the 3D pose from the cameras mounted on the HMD. Guзов et al. [21] use sensor data from IMUs placed on the subject's body and combine them with camera self-localization. They formulate an optimization problem with scene constraints, enabling the capture of long-term motions that respect scene constraints, such as foot contact with the ground. Finally, Dittadi et al. [14] propose a likelihood model that maps head and hand signals to full body poses. In our work, we adopt this scenario and empirically show that the proposed optimizer rule is competitive, both with a classic optimization baseline and a state-of-the-art likelihood model [14].

3. Method

3.1. Human body model

We represent the human body using SMPL+H [53], a differentiable function that computes mesh vertices $M(\theta, \beta) \in \mathbb{R}^{V \times 3}$, $V = 6890$, from pose θ , which includes the rotation and translation of the root and body articulation, and shape β . The shape parameter $\beta \in \mathbb{R}^{10}$ contains

the coefficients of a low dimensional PCA space, that represents different body shapes. The 52 3D joints, $\mathcal{J}(\beta)$, of a kinematic skeleton are computed from the shape parameters. The pose parameters $\theta \in \mathbb{R}^{52 \times D + 3}$ contain the parent-relative rotations of each joint, where D is the dimension of the rotation representation, and the global translation. Here, we represent rotations using the 6D rotation parameterization of Zhou et al. [77], thus $\theta \in \mathbb{R}^{52 \times 6 + 3}$. The world transformation $T_j(\theta) \in SE(3)$ of each joint j is computed by following the transformations of its parents in the kinematic tree:

$$T_j(\theta) = T_{p(j)}(\theta) * T(\theta_j, \mathcal{J}_j(\beta)), \quad (1)$$

where $p(j)$ is the index of the parent of joint j and $T(\theta_j, \mathcal{J}_j(\beta))$ is the rigid transformation of joint j relative to its parent. The articulated mesh M is computed using standard linear blend skinning (LBS), applied on the transformations T . We use \mathcal{E} to denote the set of vertex indices that form the edges of the mesh.

The main body fitting scenario we tackle in this paper is for AR/VR and from sparse inputs as illustrated in Fig. 2. We make the following assumptions

- the device head tracking system provides a 6-DoF transformation T^H , that contains the position and orientation of the *headset* in the world coordinate frame.
- the device hand tracking system gives us the orientation and position of the left and right wrist, $T^L(\theta), T^R(\theta) \in SE(3)$, and the positions of the fingertips $P_{1,\dots,5}^L(\theta), P_{1,\dots,5}^R(\theta) \in \mathbb{R}^3$ in the world coordinate frame, if and when they are in the field of view (FOV) of the HMD.

Note that $T^H(\theta) = T^{HMD} T_{j_H}(\theta)$, where j_H is the index of the head joint of SMPL+H, T^{HMD} is a fixed transform from SMPL+H head joint to the headset coordinate space (origin on the forehead). T^{HMD} can be obtained from an offline calibration phase or treated as parameters and learned from the data.

Visibility is represented by $v_L, v_R \in \{0, 1\}$ for the left and right hand respectively. We examine two scenarios of visibility: 1) Full visibility where hands are always visible and provided as input 2) Half-space visibility where everything in front of the HMD is visible. In more details, we transform the points into the coordinate frame of the headset, using T^H . All points with $z \geq 0$ are behind the headset and thus invisible. Fig. 2 right visualizes the plane that defines what is visible or not.

To sum up, the sensor data for this problem are: $D^{HMD} = \{T^H, T^L, T^R, P_{i=1,\dots,5}^L, P_{i=1,\dots,5}^R, v_L, v_R\}$. The goal is to estimate the parameters $\Theta^{HMD} = \{\theta\} \in \mathbb{R}^{315}$, i.e. pose and translation that best fit to D^{HMD} while also being a plausible solution (e.g. no floor penetration). Note that body shape β

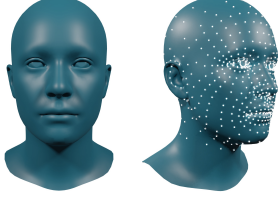


Figure 3. The template of the face model of Wood et al. [66] (blue mesh, frontal view) and the 669 dense landmarks (white dots, side view) in our 3D parametric face fitting example.

is given as input and assumed to come from a separate enrolment step.

3.2. Human face model

We represent the human face using the parametric face model proposed by Wood et al. [66]. Similar to the human body model explained in Sec. 3.1, this face model is also a differentiable function that computes mesh vertices $M(\theta, \beta, \psi) \in \mathbb{R}^{v \times 3}$, $v = 7414$, from pose θ , which includes the global translation, the rotations of $J = 4$ joints (a minimal skeleton with head, neck and two eyes), the identity blendshape coefficients $\beta \in \mathbb{R}^{256}$ and the expression blendshape coefficients $\psi \in \mathbb{R}^{233}$. The deformed mesh is defined as:

$$M(\theta, \beta, \psi) = \mathcal{LBS}(\mathcal{X}(\beta, \psi), \theta, \mathcal{J}(\beta); \mathbf{W}) \quad (2)$$

where $\mathcal{LBS}(\mathbf{X}, \theta, \mathbf{J}; \mathbf{W})$ is a standard LBS function that rotates vertex positions $\mathbf{X} \in \mathbb{R}^{v \times 3}$ about joint locations $\mathbf{J} \in \mathbb{R}^{J \times 3}$ by local joint rotations of θ , with per-vertex LBS weights $\mathbf{W} \in \mathbb{R}^{v \times J}$. Note $\mathcal{X}(\beta, \psi) : \mathbb{R}^{|\beta| \times |\psi|} \rightarrow \mathbb{R}^{v \times 3}$ deforms the template (unposed) mesh \bar{M} by applying the linear identity mesh bases \mathcal{B}_S and linear expression bases \mathcal{B}_E :

$$\mathcal{X}(\beta, \psi) = \bar{M} + \beta * \mathcal{B}_S + \psi * \mathcal{B}_E. \quad (3)$$

$\mathcal{J}(\beta)$ is computed similarly by applying the linear identity bone bases to the template joint positions.

For face fitting, we select a set of mesh vertices as the face landmarks $\mathcal{P} \in \mathbb{R}^P \times 3$, $P = 669$ (see Fig. 3 right). The input data are the corresponding 2D face landmarks $\tilde{\mathcal{Q}} \in \mathbb{R}^P \times 2$, detected using the landmark neural network proposed by Wood et al. [66] for example.

For this task, our goal is to estimate translation, joint rotations, expression and identity coefficients $\Theta^F = \{\theta, \psi, \beta\} \in \mathbb{R}^{516}$ that best fit the 2D landmarks $D^F = \tilde{\mathcal{Q}}$. We assume we are dealing with calibrated cameras and thus have access to the camera intrinsics K . $\pi(\mathcal{P}; K)$ is the perspective camera projection function used to project the 3D landmarks \mathcal{P} onto the image plane.

3.3. Data terms

The data term is a function $\mathcal{L}^D(\Theta; D)$ that measures the discrepancy between the observed inputs D (D^{HMD} or D^F)

Algorithm 1 Our neural fitting process

Require: Input data D

$$\Theta_0 = \Phi(D)$$

$$h_0 = \Phi_h(D)$$

while not converged **do**

$$\Delta\Theta_n, h_n \leftarrow f([g_{n-1}, \Theta_{n-1}], D, h_{n-1})$$

$$\Theta_n \leftarrow \Theta_{n-1} + u(\Delta\Theta_n, g_{n-1}, \Theta_{n-1})$$

end while

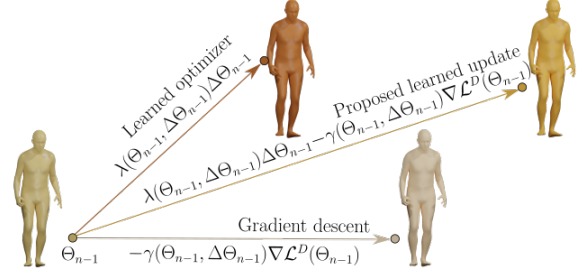


Figure 4. Existing learned optimizers update the morphable model parameters iteratively using only the network learned descent. Inspired by the classic LM algorithm, we propose to combine the network learned descent with the gradient descent with learned combination weights λ and γ .

and the parametric model evaluated at the estimated parameters Θ (Θ^{HMD} or Θ^F). In the following, variables with a hat denote inputs or observed quantities.

At n -th iteration of the fitting process, we compute both (a) the array $\mathcal{R}(\Theta_n)$ that contains all corresponding residuals of the data term \mathcal{L}^D for the current set of parameters Θ_n , and (b) the gradient $g_n = \nabla\mathcal{L}^D(\Theta_n)$.

Let $\|\cdot\|$ by any metric appropriate for $SE(3)$ [14] and $\|\cdot\|_\psi$ a robust norm [5]. In order to be able to compute residuals, we use the Frobenius norm for $\|\cdot\|$ and $\|\cdot\|_\psi$ for all the problem settings. Note that any other norm choice could be made compatible with LM, using the techniques described by Zach et al. [74].

Body fitting from HMD signals: We measure the discrepancy between the observed data D^{HMD} and the estimated model parameters Θ^{HMD} with the following data term:

$$\begin{aligned} \mathcal{L}^D(\Theta^{\text{HMD}}; D^{\text{HMD}}) = & \|\hat{T}^H, T^H(\Theta^{\text{HMD}})\| + \\ & \sum_{w \in \mathbf{L}, \mathbf{R}} v_w \left(\|\hat{T}^w, T^w(\Theta^{\text{HMD}})\| + \sum_{i=1}^5 \|\hat{P}_i^w - P_i^w(\Theta^{\text{HMD}})\|_\psi \right) \end{aligned} \quad (4)$$

Face fitting from 2D landmarks: we use the landmark re-projection error as our data term:

$$\mathcal{L}^D(\Theta^F; D^F) = \|\tilde{\mathcal{Q}} - \pi(\mathcal{P}(\Theta^F); K)\|_\psi \quad (5)$$

Note that given $\Theta^F = \{\theta, \psi, \beta\}$, the deformed 3D landmarks (a subset of mesh vertices) are computed using Eq. 2. Here we abuse notation and use $\mathcal{P}(\Theta^F)$ as such function.

3.4. Neural fitter

Our proposed neural fitter estimates the values of the parameters Θ by iteratively updating an initial estimate θ_0 , following the process described in Alg. 1. While the initial estimate Θ_0 obtained from a deep neural network might be sufficiently accurate for some applications, we will show that a careful construction of the update rule ($u(\cdot)$ in Alg. 1) leads to significant improvements after only a few iterations.

The classic Levenberg–Marquardt algorithm [38, 44], computes the parameter update $\Delta\Theta$ as the solution of: $(J^\top J + \lambda \text{diag}(J^\top J))\Delta\Theta = J^\top \mathcal{R}(\Theta)$. Increasing λ pushes the update closer to the gradient descent direction, while lowering its value brings it closer to Gauss-Newton. We draw inspiration from this and propose to compute the update as a combination of gradient descent g_n and a learned descent direction $\Delta\Theta_n$. As shown in Alg. 1, for the n -th iteration, we first use a neural network f to predict $\Delta\Theta_n$, and then apply the new update rule:

$$u(\Delta\Theta_n, g_n, \Theta_n) = \lambda \Delta\Theta_n + (-\gamma g_n) \quad (6)$$

$$\lambda(\Theta_n, \Delta\Theta_n) = f_\lambda(\mathcal{R}(\Theta_n), \mathcal{R}(\Theta_n + \Delta\Theta_n)) \quad (7)$$

$$\gamma(\Theta_n, \Delta\Theta_n) = f_\gamma(\mathcal{R}(\Theta_n), \mathcal{R}(\Theta_n + \Delta\Theta_n)) \quad (8)$$

$$\lambda, \gamma \in \mathbb{R}^{|\Theta|} \quad (9)$$

Note that λ and γ are the combination weights which are also learned using neural network f_λ, f_γ respectively. Fig. 4 contains a visualization of the individual terms of Eq. 6 and of the final combination.

3.5. Training details

Model structure: The functions f, f_λ, f_γ are implemented with a Gated Recurrent Unit (GRU) [10] and layer normalization [3]:

$$\begin{aligned} z_n &= \sigma_g(LN(W_z x) + LN(U_z h_{n-1})) \\ r_n &= \sigma_g(LN(W_r x) + LN(U_r h_{n-1})) \\ \hat{h}_n &= \phi_h(LN(W_h x) + LN(U_h(r_n \odot h_{n-1}))) \\ h_n &= (1 - z_n) \odot h_{n-1} + z_n \odot \hat{h}_n \\ \Theta_n &= W_\Theta h_n + b_\Theta \\ h_0 &= \Phi_h(D) \end{aligned} \quad (10)$$

$$(11)$$

Unless otherwise specified, we use a stack of two GRUs with 1024 units each. The functions $\Phi(), \Phi_h()$ are MLPs with two layers of 256 units, ReLU activation [47] and batch normalization (BN) [27].

Training losses: We apply a loss on the output of every step of our network:

$$\mathcal{L}(\{\Theta_n\}_{n=0}^N, \{\hat{\Theta}_n\}_{n=0}^N; D) = \sum_{i=0}^N \mathcal{L}(\Theta_i, \hat{\Theta}_i; D) \quad (12)$$

The loss \mathcal{L}_i contains the following terms:

$$\mathcal{L}_i = \lambda_M \mathcal{L}_i^M + \lambda_E \mathcal{L}_i^E + \lambda_T \mathcal{L}_i^T + \lambda_\theta \mathcal{L}_i^\theta \quad (13)$$

$$\mathcal{L}_i^M = \|\hat{M} - M\|_1 \quad (14)$$

$$\mathcal{L}_i^E = \sum_{(i,j) \in \mathcal{E}} \|(\hat{M}_i - \hat{M}_j) - (M_i - M_j)\|_1 \quad (15)$$

$$\mathcal{L}_i^T = \sum_{j=1}^J \|\hat{T}_j - T_j\|_1 \quad (16)$$

$$\mathcal{L}_i^\theta = \|\hat{R}_\theta - R_\theta\|_1 + \|\hat{t} - t\|_1 \quad (17)$$

where R_θ denotes the rotation matrices computed from the pose values θ and t is the root translation vector. See the **Sup. Mat.** for the values of $\{\lambda_M, \lambda_E, \lambda_T, \lambda_\theta, \lambda_t\}$.

Datasets: For body fitting from HMD signals, we use a subset of AMASS [42] to train and test our method. Specifically, we use CMU [9], KIT [43] and MPI-HDM05 [46], adopting the same pre-processing and training, test splits as [14]. An important difference is that we fit the neutral SMPL+H to the gendered SMPL+H data found in AMASS, to preserve correct contact with the ground and avoid the use of heuristics [52]. We attach random hand poses from the MANO [53] training set to simulate hand articulation. In all our experiments that involve SMPL+H, we use the ground-truth shape parameters β . Future work could include estimating a subset of the shape parameters corresponding to height from the position of the headset.

For face fitting from 2D landmarks, we use the face model proposed in [66] and generate a synthetic face dataset by sampling 50000 sets of parameters from the model space. For each sample, we vary pose, identity and expression of the face model. We use a perspective camera with focal length (512, 512) and principal point (256, 256) (in pixels) to project the 3D landmarks onto the image for 2D landmarks (input data). Afterwards, we randomly split this by 80/20 into training and testing sets.

Training: We implement our model in [49] and train it with a batch size of 512 on 4 GPUs using Adam [31]. We anneal the learning rate by a factor of 0.1 after 400 epochs. We apply dropout with a probability of $p = 0.5$ on the hidden states of the GRUs. We initialize the weights of the output linear layer of Eq. 10 with a gain equal to 0.01 [20].

4. Experiments

4.1. Metrics

For body fitting from HMD signals, we report the following metrics.

Vertex-to-Vertex (V2V): Since for all our data we know the correspondence between ground-truth \tilde{M} and estimated vertices M , we are able to compute the mean per-vertex error: $V2V(\tilde{M}, M) = \frac{1}{V} \sum_{i=1}^V \|\tilde{M}_i - M_i\|_2$. For SMPL+H,

Full visibility					
Method	Vertex-to-vertex (mm) ↓			Full body	GrPe.
	Full body	Head	L / R hand	JntErr (mm) ↓	(mm)↓
LM, GMM	73.1	2.9	3.2 / 3.0	49.7	70.8
LM, VAE Encoder	76.1	3.9	5.3 / 4.7	52.6	63.6
LM, GMM temporal	72.6	2.9	3.3 / 3.1	49.4	70.7
Dittadi et al. [14]	-	-	n/a	43.3	-
Ours Φ , ($N = 0$)	44.2	19.1	27.8 / 25.9	38.9	16.1
Ours ($N = 5$)	26.1	2.2	3.0 / 3.3	18.1	12.5

Half-space visibility					
	Vertex-to-vertex (mm) ↓			Full body	GrPe.
	Full body	Head	L / R hand	JntErr (mm) ↓	(mm)↓
LM, GMM	116.2	3.4	5.6 / 5.3	137.26	74.0
LM, VAE Encoder	119.3	4.1	8.7 / 7.6	140.5	66.7
LM, GMM Temporal	113.3	3.4	6.8 / 6.5	132.1	73.5
Ours Φ , ($N = 0$)	69.7	22.7	32.1 / 29.9	84.9	20.1
Ours ($N = 5$)	49.9	3.2	3.1 / 3.7	62.1	15.5

Table 1. Fitting SMPL+H to simulated sequences of HMD data. We report full body, part and ground penetration metrics. Our proposed fitter outperforms the classical optimization baselines on the full body and ground penetration metrics, with similar or better performance on the part metrics.

in addition to the full mesh error, we report error values for parts of the body, namely the head and the hands, and the joints. The **3D per-joint error (JntErr)** is equal to: $\text{JntErr}(\tilde{\mathcal{J}}, \mathcal{J}) = \frac{1}{52} \sum_{i=1}^{52} \|\tilde{\mathcal{J}}_i - \mathcal{J}_i\|_2$. A visualization of the selected parts is included in the **Sup. Mat.**

Ground penetration (GrPe.): We report the average distance to the ground plane for all vertices below ground [73]: $\text{GrPe.}(M) = \frac{1}{|S|} \sum_{n \in S} |d_{\text{gnd}}(M_i)|$, where $d_{\text{gnd}}(M_i) = M_i \cdot n_{\text{gnd}}$ and $S = \{i \mid d_{\text{gnd}}(M_i) < 0\}$.

For face fitting from 2D landmarks, we use the above **Vertex-to-Vertex** metric and the mean **3D landmark error (LdmkErr)**: $\text{LdmkErr}(\tilde{\mathcal{P}}, \mathcal{P}) = \frac{1}{P} \sum_{i=1}^P \|\tilde{\mathcal{P}}_i - \mathcal{P}_i\|_2$.

4.2. Quantitative evaluation

4.2.1 Fitting the body to HMD data

We start by comparing our proposed learned optimizer with a standard optimization pipeline on the problem of fitting SMPL+H to sparse HMD signals described in Sec. 3.1. The optimization baseline minimizes the energy with data term (\mathcal{L}^D in Eq. 4), gravity term, prior term and temporal term to estimate the parameters $\Theta_{1,\dots,T}$ of a sequence of length T :

$$\begin{aligned}
\mathcal{L}^O(\Theta^{\text{HMD}}) &= \mathcal{L}^D(\Theta^{\text{HMD}}; D^{\text{HMD}}) + \mathcal{L}^G + \mathcal{L}^{\theta}_{\text{prior}} + \mathcal{L}^T \\
\mathcal{L}^G(\Theta^{\text{HMD}}) &= 1 - \frac{T_{\text{pelvis}}(1, : 3) \cdot \mathbf{u}}{\|T_{\text{pelvis}}(1, : 3)\|_2 \|\mathbf{u}\|_2}, \mathbf{u} = (0, 1, 0) \\
\mathcal{L}^T(\Theta^{\text{HMD}}) &= \sum_{t=1}^{T-1} \|T_{t+1}(\Theta_{t+1}^{\text{HMD}}) - T_t(\Theta_t^{\text{HMD}})\|
\end{aligned} \tag{18}$$

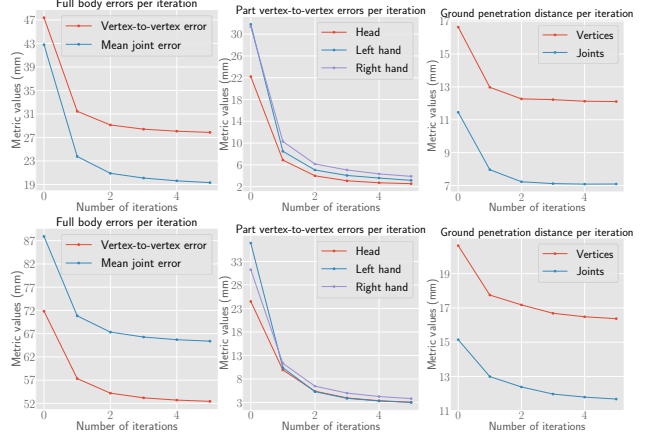


Figure 5. Errors per iteration when fitting SMPL+H to HMD data. The top row corresponds to the full visibility scenario, while the bottom row contains the data for the half-space setup. From left to right: 1) Full body vertex and joint errors, 2) head, left and right hand vertex-to-vertex errors and 3) vertex and joint ground distance, computed on the set of points below ground.

We use two different pose priors, a GMM [7] and a VAE encoder $\mathcal{E}()$ [51]:

$$\mathcal{L}_{\text{GMM}}^{\theta} = -\min_j \log(w_j \mathcal{N}(\theta; \mu_{\theta,j}, \Sigma_{\theta,j})) \tag{19}$$

$$\mathcal{L}_{\text{VAE}}^{\theta} = \text{Neg. Log-Likelihood}(\mathcal{N}(\mathcal{E}(\theta), \mathcal{I})) \tag{20}$$

We minimize the loss above using L-BFGS [48, Ch. 7.2] for 120 iterations on the test split of the MoCap data. We choose L-BFGS instead of Levenberg-Marquardt, since PyTorch currently lacks the feature to efficiently compute jacobians, without having to resort to multiple backward passes for derivative computations. We report the results for the full and half-space visibility in Tab. 1. This table contains the metrics of Section 4.1 for the optimization approach, the method of Dittadi et al. [14], only for the full visibility scenario, and our learned fitter. Our method outperforms the baselines in terms of full-body and penetration metrics and shows competitive performance w.r.t. to the part metrics. While regression only methods can produce competitive results, they lack a feedback mechanism to inform them how closely they match the input data.

Runtime: our method (PyTorch) runs at *150 ms* per frame on a P100 GPU, while the baseline optimization method (PyTorch) above requires *520 ms*, on the same hardware. We are aware that a highly optimized real-time version of the latter exists and runs at *0.8 ms* per frame, performing at least 3 LM iterations, but it requires investing significant effort into a problem specific C++ codebase.

Fig. 5 contains the metrics per iteration, averaged across the entire test dataset, for our learned fitter. There we see that the proposed model is able to aggressively optimize the target data term and quickly converge to the minimum.

Method	Weight sharing				GrPe. (mm)↓
	Vertex-to-vertex (mm) ↓			Full body JntErr (mm) ↓	
	Full body	Head	L / R hand		
Shared weights	52.3	3.5	3.6 / 3.7	64.1	18.2
Per-step weights	49.9	3.2	3.1 / 3.7	62.1	15.5

Table 2. Although the use of different weights per-optimization step leads to a N-fold parameter increase, it helps better fit the head and reduces ground penetration (GrPe.).

Ablation: We perform all our ablations on the problem of fitting SMPL+H to HMD signals, using the half-space visibility setting shown in Fig. 2. Unless otherwise stated, all numbers are reported after running the initial regressor and the learned fitter for 5 iterations.

We investigate whether it is beneficial to have shared weights across model iterations or to have a separate instance per optimization step. Table 2 shows that this can help reduce the errors, at the cost of a N-fold increase in memory.

Afterwards, we investigate the effect of the type and structure of the network. Specifically, we replace the GRU with the feed-forward network with skip connections [24, 60] of Song et al. [59]. Furthermore, we also train a version of our fitter with a single GRU with 1024 units, instead of a two stack networks with 1024 units. Table 3 shows that the GRU is the better module for this type of problem, thanks to its internal memory. This is very much in line with how many popular continuous optimizers work.

The next step is to compare the update rule of Eq. 6 with a learned fitter trained to update the parameters using only the network update. We report the results of this evaluation in Tab. 4. This experiment confirms that using the gradient for our update is more beneficial than the raw network or a more constrained update.

Next, we look at the value of the gradient descent learning rate γ . We compare the proposed learned gradient descent update with using a constant value. Table 5 shows that performance gracefully degrades when using the constant learning value. Therefore, it is a valid alternative for decreasing the computational cost, without a significant performance drop.

Finally, we present some qualitative results in Fig. 7. Notice how the learned fitter corrects the head pose and hand articulation of the initial predictions.

4.2.2 Fitting face to 2D landmarks

We compare our proposed learned optimizer with a C++ production grade solution that uses LM to solve the face fitting problem described in Sec. 3.2. Given the per-image 2D landmarks as input, the optimization baseline minimizes the energy with data term (\mathcal{L}^D in Eq. 5) and a simple regular-

Method	Network structure (non-shared weights)				
	Vertex-to-vertex (mm) ↓			Full body	GrPe.
	Full body	Head	L / R hand	JntErr (mm) ↓	(mm)↓
ResNet	65.3	6.8	7.3 / 7.6	73.1	16.2
GRU (1024)	53.6	3.7	3.4 / 4.0	66.1	15.1
GRU (1024, 1024)	49.9	3.2	3.1 / 3.7	62.1	15.5

Table 3. Comparison of our GRU-based fitter with the ResNet [24, 60] based of Song et al. [59]. Thanks to its internal memory and gating mechanism, the GRU is able to more effectively fit the target data. Stacking multiple GRUs further improves performance, at the cost of increased memory and runtime.

Method	Update rule				GrPe. (mm)↓
	Vertex-to-vertex (mm) ↓			Full body JntErr (mm) ↓	
	Full body	Head	L / R hand		
+ $\Delta\Theta_n$	53.8	14.7	7.8 / 7.9	66.3	15.8
+Eq. 6	49.9	3.2	3.1 / 3.7	62.1	15.5

Table 4. Comparison of our proposed update rule (Eq. 6) with the pure network update $\Delta\Theta_n$. Our combination of the network output and the gradients of \mathcal{L}^D improve the results for all metrics.

Method	Learning rate γ				
	Vertex-to-vertex (mm) \downarrow			Full body	GrPe.
	Full body	Head	L / R hand	JntErr (mm) \downarrow	(mm) \downarrow
Constant $\gamma=1e-4$	51.9	3.5	3.8 / 4.6	64.2	15.5
Learned γ	49.9	3.2	3.1 / 3.7	62.1	15.5

Table 5. While the use of learned learning rate vector γ can help further improve the metrics, this table shows that a constant value performs almost as well. Therefore it might be an option if we would like to decrease the computational cost of the method, without sacrificing much in terms of performance.

ization term to estimate $\Theta^F = \{\theta, \psi, \beta\}$:

$$\mathcal{L}^O(\Theta^F) = \mathcal{L}^D(\Theta^F; D^F) + \mathbf{w} * \|\Theta^F\|_2 \quad (21)$$

\mathbf{w} contains the different regularization weights for θ, ψ, β , which are tuned manually for the best baseline result.

Tab. 6 shows the quantitative comparison and ours are better in almost all metrics. Note that fitting 3D model to a single 2D image is likely to have offset in depth direction [34], which explains the larger value in absolute errors (Wo. columns). After re-alignment (Aff. columns), the gap is much smaller. See Fig. 6 for a qualitative comparison.

Runtime: for face fitting, the baseline optimization is in C++ and thus for a fair comparison, we only compare the time it takes to compute the parameter update given residuals and jacobians (per-iteration). Computing the values of the learned parameter update (ours, using PyTorch) takes 12 ms on a P100 GPU, while computing the LM update (baseline, C++) requires 34.7 ms. Note that this baseline LM update only requires 0.8 ms on a laptop CPU when optimizing over 100 free variables. The difference comes from the



Figure 6. Fitting the pose, expression and identity parameters of a 3D face model [66] to dense 2D landmarks: 1) target 2D landmarks, 2) LM fitter results, 3) our fitter result, 4) ground-truth.

Method	Vertex-to-vertex (mm) ↓				LdmkErr (mm) ↓	
	Face		Head		Wo.	Aff.
	Wo.	Aff.	Wo.	Aff.		
LM	34.4	3.7	33.8	5.3	33.8	3.4
Ours	7.9	3.5	8.5	4.1	8.0	3.7

Table 6. Fitting 3D face model [66] to 2D facial landmark data. We report the V2V metrics on the whole head and the face (excluding neck because landmarks are usually undefined there), and also the 3D landmark metrics (LdmkErr). Aff. means re-aligning the mesh by undoing scale, rotation, and translation before metrication [18] while Wo. directly uses the fitter’s prediction. Both methods run for max. 5 iterations. Our learned fitter equals or outperforms LM on all metrics.

fact that the complexity of LM is cubic in the number of free variables in the optimization problem.

4.3. Discussion

If we apply the proposed method to a sequence of data, we will get plausible per-frame results, but the overall motion will be implausible. Since the model is trained on a per-frame basis and lacks temporal context, it cannot learn the proper dynamics present in temporal data. Thus, limbs in successive frames will move unnaturally, with large jumps or jitter. Future extensions of this work should therefore explore how to best use past frames and inputs. This could be coupled with a physics based approach, either as part of a controller [73] or using explicit physical losses [68] in \mathcal{L}^D . Finally, another interesting direction is the use of more effective parameterizations for the per-step weights [13, 25].

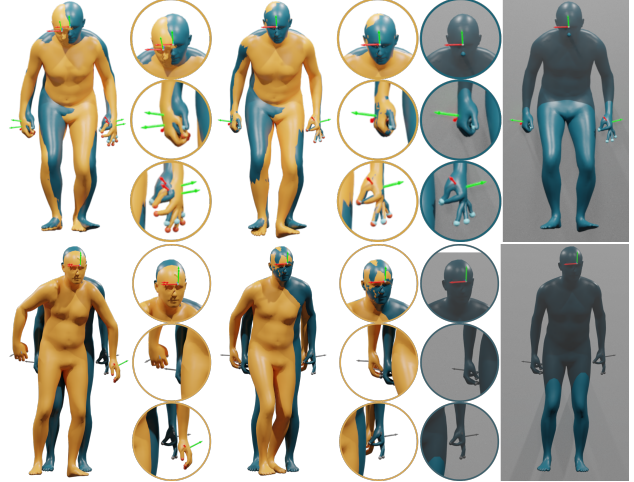


Figure 7. Bodies estimated from HMD signals with our learned SMPL+H fitter (half-space visibility). From left to right: 1) Initial Φ output (in yellow), 2) iteration $N = 5$ of our fitter (in yellow), 3) ground-truth overlay (in blue). Points that are greyed out are outside of the field of view, e.g. both hands in the second row. Our learned optimizer successfully fits the target head and hands data and produces plausible poses for the full 3D body. In the second row, hands are outside of FOV and thus not perfectly fitted. Best viewed in color.

Social impact: Accurate tracking is a necessary prerequisite for the next generation of communication and entertainment through virtual and augmented reality. Learned optimizers represent a promising avenue to realize this potential. However, it can also be used for surveillance and tracking of private activities of an individual, if the corresponding sensor is compromised.

5. Conclusion

In this work, we propose a learned parameter update rule inspired from classic optimization algorithms that outperforms the pure network update and is competitive with standard optimization baselines. We demonstrate the utility of our algorithm on two different problem sets, fitting the 3D body and hands to sparse HMD signals and fitting the face to dense 2D landmarks. Learned optimizers combine the advantages of classic optimization and regression approaches. They greatly simplify the development process for new problems, since the parameter priors are directly learned from the data, without manual specification and tuning, and they run at interactive speeds, thanks to the development of specialized software for neural network inference. Thus, we believe that our proposed optimizer will be useful for any applications that involve generative model fitting.

Acknowledgement: We thank Pashmina Cameron, Sadegh Aliakbarian, Tom Cashman, Darren Cosker and Andrew Fitzgibbon for useful discussions and proof reading.

References

- [1] Jonas Adler and Ozan Öktem. Solving ill-posed inverse problems using iterative deep neural networks. *Inverse Problems*, 33(12):124007, 2017. 2
- [2] Marcin Andrychowicz, Misha Denil, Sergio Gómez, Matthew W Hoffman, David Pfau, Tom Schaul, Brendan Shillingford, and Nando de Freitas. Learning to learn by gradient descent by gradient descent. In D. Lee, M. Sugiyama, U. Luxburg, I. Guyon, and R. Garnett, editors, *NeurIPS*, volume 29. Curran Associates, Inc., 2016. 2
- [3] Jimmy Lei Ba, Jamie Ryan Kiros, and Geoffrey E Hinton. Layer normalization. *arXiv preprint arXiv:1607.06450*, 2016. 5
- [4] Seungryul Baek, Kwang In Kim, and Tae-Kyun Kim. Pushing the envelope for RGB-based dense 3D hand pose estimation via neural rendering. In *CVPR*, pages 1067–1076, 2019. 2
- [5] Jonathan T. Barron. A general and adaptive robust loss function. *CVPR*, 2019. 4
- [6] Volker Blanz and Thomas Vetter. A morphable model for the synthesis of 3D faces. In *ACM Transactions on Graphics (Proceedings of SIGGRAPH)*, pages 187–194, 1999. 2
- [7] Federica Bogo, Angjoo Kanazawa, Christoph Lassner, Peter Gehler, Javier Romero, and Michael J. Black. Keep it SMPL: Automatic estimation of 3D human pose and shape from a single image. In *ECCV, Lecture Notes in Computer Science*, pages 561–578. Springer International Publishing, Oct. 2016. 2, 6
- [8] Adnane Boukhayma, Rodrigo de Bem, and Philip H.S. Torr. 3D hand shape and pose from images in the wild. In *CVPR*, pages 10843–10852, 2019. 2
- [9] Carnegie Mellon University. CMU MoCap Dataset. 5
- [10] Kyunghyun Cho, Bart van Merriënboer, Caglar Gulcehre, Dzmitry Bahdanau, Fethi Bougares, Holger Schwenk, and Yoshua Bengio. Learning phrase representations using RNN encoder–decoder for statistical machine translation. In *Proceedings of the 2014 Conference on Empirical Methods in Natural Language Processing (EMNLP)*, pages 1724–1734, Doha, Qatar, Oct. 2014. Association for Computational Linguistics. 5
- [11] Hongsuk Choi, Gyeongsik Moon, and Kyoung Mu Lee. Beyond Static Features for Temporally Consistent 3D Human Pose and Shape from a Video. In *CVPR*, 2021. 2
- [12] Vasileios Choutas, Georgios Pavlakos, Timo Bolkart, Dimitrios Tzionas, and Michael J. Black. Monocular Expressive Body Regression through Body-Driven Attention. In *ECCV*, pages 20–40, 2020. 2
- [13] Javier Dehesa, Andrew Vidler, Julian Padget, and Christof Lutteroth. Grid-Functioned Neural Networks. In Marina Meila and Tong Zhang, editors, *ICML*, volume 139 of *Proceedings of Machine Learning Research*, pages 2559–2567. PMLR, 18–24 Jul 2021. 8
- [14] Andrea Dittadi, Sebastian Dziadzio, Darren Cosker, Ben Lundell, Thomas J. Cashman, and Jamie Shotton. Full-Body Motion From a Single Head-Mounted Device: Generating SMPL Poses From Partial Observations. In *ICCV*, pages 11687–11697, October 2021. 3, 4, 5, 6
- [15] Zijian Dong, Jie Song, Xu Chen, Chen Guo, and Otmar Hilliges. Shape-aware Multi-Person Pose Estimation from Multi-View Images. In *ICCV*, pages 11158–11168, 2021. 3
- [16] Bernhard Egger, William A. P. Smith, Ayush Tewari, Stefanie Wuhler, Michael Zollhoefer, Thabo Beeler, Florian Bernard, Timo Bolkart, Adam Kortylewski, Sami Romdhani, Christian Theobalt, Volker Blanz, and Thomas Vetter. 3D Morphable Face Models - Past, Present and Future. *ACM Transactions on Graphics*, 39(5), Aug. 2020. 2
- [17] Taosha Fan, Kalyan Vasudev Alwala, Donglai Xiang, Weipeng Xu, Todd Murphey, and Mustafa Mukadam. Revitalizing Optimization for 3D Human Pose and Shape Estimation: A Sparse Constrained Formulation. In *ICCV*, pages 11457–11466, October 2021. 2
- [18] Yao Feng, Vasileios Choutas, Timo Bolkart, Dimitrios Tzionas, and Michael J. Black. Collaborative regression of expressive bodies using moderation. In *International Conference on 3D Vision (3DV)*, 2021. 2, 8
- [19] John Flynn, Michael Broxton, Paul Debevec, Matthew DuVall, Graham Fyffe, Ryan Overbeck, Noah Snavely, and Richard Tucker. Deepview: View synthesis with learned gradient descent. In *CVPR*, pages 2367–2376, 2019. 2
- [20] Xavier Glorot and Yoshua Bengio. Understanding the difficulty of training deep feedforward neural networks. In *Proceedings of the Thirteenth International Conference on Artificial Intelligence and Statistics*, pages 249–256. JMLR Workshop and Conference Proceedings, 2010. 5
- [21] Vladimir Guzov, Aymen Mir, Torsten Sattler, and Gerard Pons-Moll. Human POSEitioning System (HPS): 3D Human Pose Estimation and Self-Localization in Large Scenes From Body-Mounted Sensors. In *CVPR*, pages 4318–4329, June 2021. 3
- [22] Mohamed Hassan, Vasileios Choutas, Dimitrios Tzionas, and Michael J. Black. Resolving 3D human pose ambiguities with 3D scene constraints. In *ICCV*, pages 2282–2292, Oct. 2019. 2
- [23] Yana Hasson, Gül Varol, Dimitrios Tzionas, Igor Kaleyvtykh, Michael J. Black, Ivan Laptev, and Cordelia Schmid. Learning Joint Reconstruction of Hands and Manipulated Objects. In *CVPR*, pages 11807–11816, 2019. 2
- [24] Kaiming He, Xiangyu Zhang, Shaoqing Ren, and Jian Sun. Deep residual learning for image recognition. In *CVPR*, pages 770–778, 2016. 7
- [25] Daniel Holden, Taku Komura, and Jun Saito. Phase-Functioned Neural Networks for Character Control. *ACM Transactions on Graphics*, 36(4), jul 2017. 8
- [26] Christian Igel, Marc Toussaint, and Wan Weishui. Rprop using the natural gradient. In Detlef H. Mache, József Szabados, and Marcel G. de Bruin, editors, *Trends and Applications in Constructive Approximation*, pages 259–272, Basel, 2005. Birkhäuser Basel. 2
- [27] Sergey Ioffe and Christian Szegedy. Batch normalization: Accelerating deep network training by reducing internal covariate shift. In *ICLR*, pages 448–456. PMLR, 2015. 5
- [28] Hanbyul Joo, Natalia Neverova, and Andrea Vedaldi. Exemplar Fine-Tuning for 3D Human Pose Fitting Towards In-the-Wild 3D Human Pose Estimation. In *3DV*, 2021. 2
- [29] Hanbyul Joo, Tomas Simon, and Yaser Sheikh. Total capture: A 3D deformation model for tracking faces, hands, and bodies. In *CVPR*, pages 8320–8329, 2018. 2
- [30] Manuel Kaufmann, Yi Zhao, Chengcheng Tang, Lingling

- Tao, Christopher Twigg, Jie Song, Robert Wang, and Otmar Hilliges. EM-POSE: 3D Human Pose Estimation From Sparse Electromagnetic Trackers. In *ICCV*, pages 11510–11520, 2021. 2
- [31] Diederik P. Kingma and Jimmy Ba. Adam: A method for stochastic optimization. In Yoshua Bengio and Yann LeCun, editors, *ICLR*, 2015. 5
- [32] Muhammed Kocabas, Nikos Athanasiou, and Michael J. Black. VIBE: Video inference for human body pose and shape estimation. In *Proceedings IEEE Conf. on Computer Vision and Pattern Recognition (CVPR)*, pages 5252–5262. IEEE, June 2020. 2
- [33] Muhammed Kocabas, Chun-Hao P. Huang, Otmar Hilliges, and Michael J. Black. PARE: Part attention regressor for 3D human body estimation. In *ICCV*, pages 11127–11137, October 2021. 2
- [34] Muhammed Kocabas, Chun-Hao P. Huang, Joachim Tesch, Lea Müller, Otmar Hilliges, and Michael J. Black. SPEC: Seeing people in the wild with an estimated camera. In *ICCV*, pages 11035–11045, Oct. 2021. 7
- [35] Filippos Kokkinos and Iasonas Kokkinos. To The Point: Correspondence-driven monocular 3D category reconstruction. In *NeurIPS*, 2021. 2
- [36] Nikos Kolotouros, Georgios Pavlakos, Michael J. Black, and Kostas Daniilidis. Learning to reconstruct 3D human pose and shape via Model-Fitting in the loop. In *ICCV*, October 2019. 2
- [37] Nikos Kolotouros, Georgios Pavlakos, Dinesh Jayaraman, and Kostas Daniilidis. Probabilistic modeling for human mesh recovery. In *ICCV*, 2021. 2
- [38] Kenneth Levenberg. A method for the solution of certain non-linear problems in least squares. *Quarterly of applied mathematics*, 2(2):164–168, 1944. 2, 5
- [39] Jiefeng Li, Chao Xu, Zhicun Chen, Siyuan Bian, Lixin Yang, and Cewu Lu. HybriK: A Hybrid Analytical-Neural Inverse Kinematics Solution for 3D Human Pose and Shape Estimation. In *CVPR*, pages 3383–3393, 2021. 2
- [40] Matthew Loper, Naureen Mahmood, Javier Romero, Gerard Pons-Moll, and Michael J. Black. SMPL: A skinned multi-person linear model. *ACM Transactions on Graphics (Proceedings of SIGGRAPH Asia)*, 34(6):248:1–248:16, Oct. 2015. 2
- [41] Zhaoyang Lv, Frank Dellaert, James M Rehg, and Andreas Geiger. Taking a deeper look at the inverse compositional algorithm. In *CVPR*, pages 4581–4590, 2019. 2
- [42] Naureen Mahmood, Nima Ghorbani, Nikolaus F. Troje, Gerard Pons-Moll, and Michael J. Black. AMASS: Archive of motion capture as surface shapes. In *ICCV*, pages 5442–5451, Oct. 2019. 2, 3, 5
- [43] C. Mandery, Ö. Terlemez, M. Do, N. Vahrenkamp, and T. Asfour. The KIT whole-body human motion database. In *2015 International Conference on Advanced Robotics (ICAR)*, pages 329–336, July 2015. 5
- [44] Donald W Marquardt. An algorithm for least-squares estimation of nonlinear parameters. *Journal of the society for Industrial and Applied Mathematics*, 11(2):431–441, 1963. 2, 5
- [45] Franziska Mueller, Micah Davis, Florian Bernard, Oleksandr Sotnychenko, Mickael Verschoor, Miguel A. Otaduy, Dan Casas, and Christian Theobalt. Real-time pose and shape reconstruction of two interacting hands with a single depth camera. *ACM Trans. Graph.*, 38(4), jul 2019. 2
- [46] M. Müller, T. Röder, M. Clausen, B. Eberhardt, B. Krüger, and A. Weber. Documentation mocap database HDM05. Technical Report CG-2007-2, Universität Bonn, June 2007. 5
- [47] Vinod Nair and Geoffrey E Hinton. Rectified linear units improve restricted boltzmann machines. In *ICML*, 2010. 5
- [48] Jorge Nocedal and Stephen J. Wright. *Numerical Optimization*. Springer, New York, NY, USA, second edition, 2006. 6
- [49] Adam Paszke, Sam Gross, Francisco Massa, Adam Lerer, James Bradbury, Gregory Chanan, Trevor Killeen, Zeming Lin, Natalia Gimelshein, Luca Antiga, Alban Desmaison, Andreas Kopf, Edward Yang, Zachary DeVito, Martin Raison, Alykhan Tejani, Sasank Chilamkurthy, Benoit Steiner, Lu Fang, Junjie Bai, and Soumith Chintala. Pytorch: An imperative style, high-performance deep learning library. In H. Wallach, H. Larochelle, A. Beygelzimer, F. d’Alché-Buc, E. Fox, and R. Garnett, editors, *Advances in Neural Information Processing Systems 32*, pages 8024–8035. Curran Associates, Inc., 2019. 5
- [50] Priyanka Patel, Chun-Hao P. Huang, Joachim Tesch, David T. Hoffmann, Shashank Tripathi, and Michael J. Black. AGORA: Avatars in geography optimized for regression analysis. In *CVPR*, June 2021. 2
- [51] Georgios Pavlakos, Vasileios Choutas, Nima Ghorbani, Timo Bolkart, Ahmed A. A. Osman, Dimitrios Tzionas, and Michael J. Black. Expressive body capture: 3D hands, face, and body from a single image. In *CVPR*, pages 10975–10985, 2019. 2, 6
- [52] Davis Remppe, Tolga Birdal, Aaron Hertzmann, Jimei Yang, Srinath Sridhar, and Leonidas J. Guibas. HuMoR: 3D Human Motion Model for Robust Pose Estimation. In *ICCV*, 2021. 5
- [53] Javier Romero, Dimitrios Tzionas, and Michael J. Black. Embodied hands: Modeling and capturing hands and bodies together. *ACM Trans. Graph.*, (Proc. SIGGRAPH Asia), 36(6), Nov. 2017. 2, 3, 5
- [54] Yu Rong, Takaaki Shiratori, and Hanbyul Joo. Frankmocap: A monocular 3d whole-body pose estimation system via regression and integration. In *IEEE International Conference on Computer Vision Workshops*, 2021. 2
- [55] Jürgen Schmidhuber. Learning to control fast-weight memories: An alternative to dynamic recurrent networks. *Neural Computation*, 4(1):131–139, 1992. 2
- [56] Jürgen Schmidhuber. A neural network that embeds its own meta-levels. In *IEEE International Conference on Neural Networks*, pages 407–412. IEEE, 1993. 2
- [57] Michael Seeber, Roi Poranne, Marc Pollefeys, and Martin Oswald. Realistichands: A hybrid model for 3d hand reconstruction. In *3DV*, Oct. 2021. 2
- [58] Jingjing Shen, Thomas J. Cashman, Qi Ye, Tim Hutton, Toby Sharp, Federica Bogo, Andrew William Fitzgibbon, and Jamie Shotton. The Phong Surface: Efficient 3D Model Fitting using Lifted Optimization. In *ECCV*, Oct. 2020. 2
- [59] Jie Song, Xu Chen, and Otmar Hilliges. Human Body Model Fitting by Learned Gradient Descent. In Andrea Vedaldi, Horst Bischof, Thomas Brox, and Jan-Michael Frahm, edi-

- tors, *ECCV*, pages 744–760, Cham, 2020. Springer International Publishing. [2](#), [7](#)
- [60] Rupesh K Srivastava, Klaus Greff, and Jürgen Schmidhuber. Training very deep networks. In C. Cortes, N. Lawrence, D. Lee, M. Sugiyama, and R. Garnett, editors, *NeurIPS*, volume 28. Curran Associates, Inc., 2015. [7](#)
- [61] Jonathan Taylor, Lucas Bordeaux, Thomas Cashman, Bob Corish, Cem Keskin, Toby Sharp, Eduardo Soto, David Sweeney, Julien Valentin, Benjamin Luff, Arran Topalian, Erroll Wood, Sameh Khamis, Pushmeet Kohli, Shahram Izadi, Richard Banks, Andrew Fitzgibbon, and Jamie Shotton. Efficient and precise interactive hand tracking through joint, continuous optimization of pose and correspondences. *ACM Transactions on Graphics*, 35(4), July 2016. [2](#)
- [62] Denis Tomè, Thiemo Alldieck, Patrick Peluse, Gerard Pons-Moll, Lourdes Agapito, Hernán Badino, and Fernando De la Torre. SelfPose: 3D Egocentric Pose Estimation from a Headset Mounted Camera. *IEEE TPAMI*, pages 1–1, 2020. [3](#)
- [63] Denis Tome, Patrick Peluse, Lourdes Agapito, and Hernan Badino. xR-EgoPose: Egocentric 3D Human Pose from an HMD Camera. In *ICCV*, pages 7728–7738, 2019. [3](#)
- [64] Christoph Vogel and Thomas Pock. A primal dual network for low-level vision problems. In Volker Roth and Thomas Vetter, editors, *Pattern Recognition*, pages 189–202, Cham, 2017. Springer International Publishing. [2](#)
- [65] Timo von Marcard, Roberto Henschel, Michael Black, Bodo Rosenhahn, and Gerard Pons-Moll. Recovering Accurate 3D Human Pose in The Wild Using IMUs and a Moving Camera. In *ECCV*, sep 2018. [2](#)
- [66] Erroll Wood, Tadas Baltrušaitis, Charlie Hewitt, Sebastian Dziadzio, Matthew Johnson, Virginia Estellers, Thomas J. Cashman, and Jamie Shotton. Fake It Till You Make It: Face Analysis in the Wild Using Synthetic Data Alone. In *ICCV*, pages 3681–3691, October 2021. [4](#), [5](#), [8](#)
- [67] Donglai Xiang, Hanbyul Joo, and Yaser Sheikh. Monocular Total Capture: Posing Face, Body, and Hands in the Wild. In *CVPR*, pages 10965–10974, 2019. [2](#)
- [68] Kevin Xie, Tingwu Wang, Umar Iqbal, Yunrong Guo, Sanja Fidler, and Florian Shkurti. Physics-Based Human Motion Estimation and Synthesis From Videos. In *ICCV*, pages 11532–11541, October 2021. [8](#)
- [69] Hongyi Xu, Eduard Gabriel Bazavan, Andrei Zanfir, William T. Freeman, Rahul Sukthankar, and Cristian Sminchisescu. GHUM & GHUML: Generative 3D human shape and articulated pose models. In *CVPR*, pages 6183–6192, 2020. [2](#)
- [70] Dongseok Yang, Doyeon Kim, and Sung-Hee Lee. LoBSTr: Real-time Lower-body Pose Prediction from Sparse Upper-body Tracking Signals. *Computer Graphics Forum*, 2021. [3](#)
- [71] Ye Yuan and Kris Kitani. Ego-pose estimation and forecasting as real-time pd control. In *Proceedings of the IEEE International Conference on Computer Vision (ICCV)*, pages 10082–10092, 2019. [3](#)
- [72] Ye Yuan and Kris M. Kitani. 3D Ego-Pose Estimation via Imitation Learning. In *ECCV*, pages 763 – 778, September 2018. [3](#)
- [73] Ye Yuan, Shih-En Wei, Tomas Simon, Kris Kitani, and Jason Saragih. SimPoE: Simulated Character Control for 3D Human Pose Estimation. In *CVPR*, 2021. [2](#), [6](#), [8](#)
- [74] Christopher Zach. Robust bundle adjustment revisited. In David Fleet, Tomas Pajdla, Bernt Schiele, and Tinne Tuytelaars, editors, *ECCV*, pages 772–787, Cham, 2014. Springer International Publishing. [4](#)
- [75] Andrei Zanfir, Eduard Gabriel Bazavan, Mihai Zanfir, William T. Freeman, Rahul Sukthankar, and Cristian Sminchisescu. Neural Descent for Visual 3D Human Pose and Shape. In *CVPR*, pages 14484–14493, June 2021. [2](#)
- [76] Hongwen Zhang, Yating Tian, Xinchu Zhou, Wanli Ouyang, Yebin Liu, Limin Wang, and Zhenan Sun. PyMAF: 3D human pose and shape regression with pyramidal mesh alignment feedback loop. In *Proceedings of the IEEE International Conference on Computer Vision*, 2021. [2](#)
- [77] Yi Zhou, Connelly Barnes, Jingwan Lu, Jimei Yang, and Hao Li. On the continuity of rotation representations in neural networks. In *CVPR*, June 2019. [3](#)

Appendices

A. Qualitative comparisons

We present a qualitative comparison of the proposed learned optimizer with a classic optimization-based method in Fig. 8. Without explicit hand-crafted constraints, the classic approach cannot resolve problems such as ground-floor penetration. Formulating a term to represent this constraint is not a trivial process. Furthermore, tuning the relative weight of this term to avoid under-fitting the data term is not a trivial process. Our proposed method on the other hand can learn to handle these constraints directly from data, without any heuristics.

B. Hyper-parameters

We use the following values for the weights of the training losses: $\lambda_M = 1000$, $\lambda_{\mathcal{E}} = 1000$, $\lambda_T = 100$, $\lambda_{\theta} = 1$, $\lambda_t = 100$.

C. Analyzing update rule

To investigate the behavior of the different components of Eq. 6 we look at the norms of each component for a subset of the variables. Specifically, we compute the average L_2 norm for the gradient $\|g_n\|_2$, the predicted learning rate $\|\gamma\|_2$, damping $\|\lambda\|_2$ and the predicted parameter update $\|\Delta\Theta_n\|_2$ for the root rotation and translation across the entire test dataset. Figure 9 contains the per-iteration plots for all the above values.

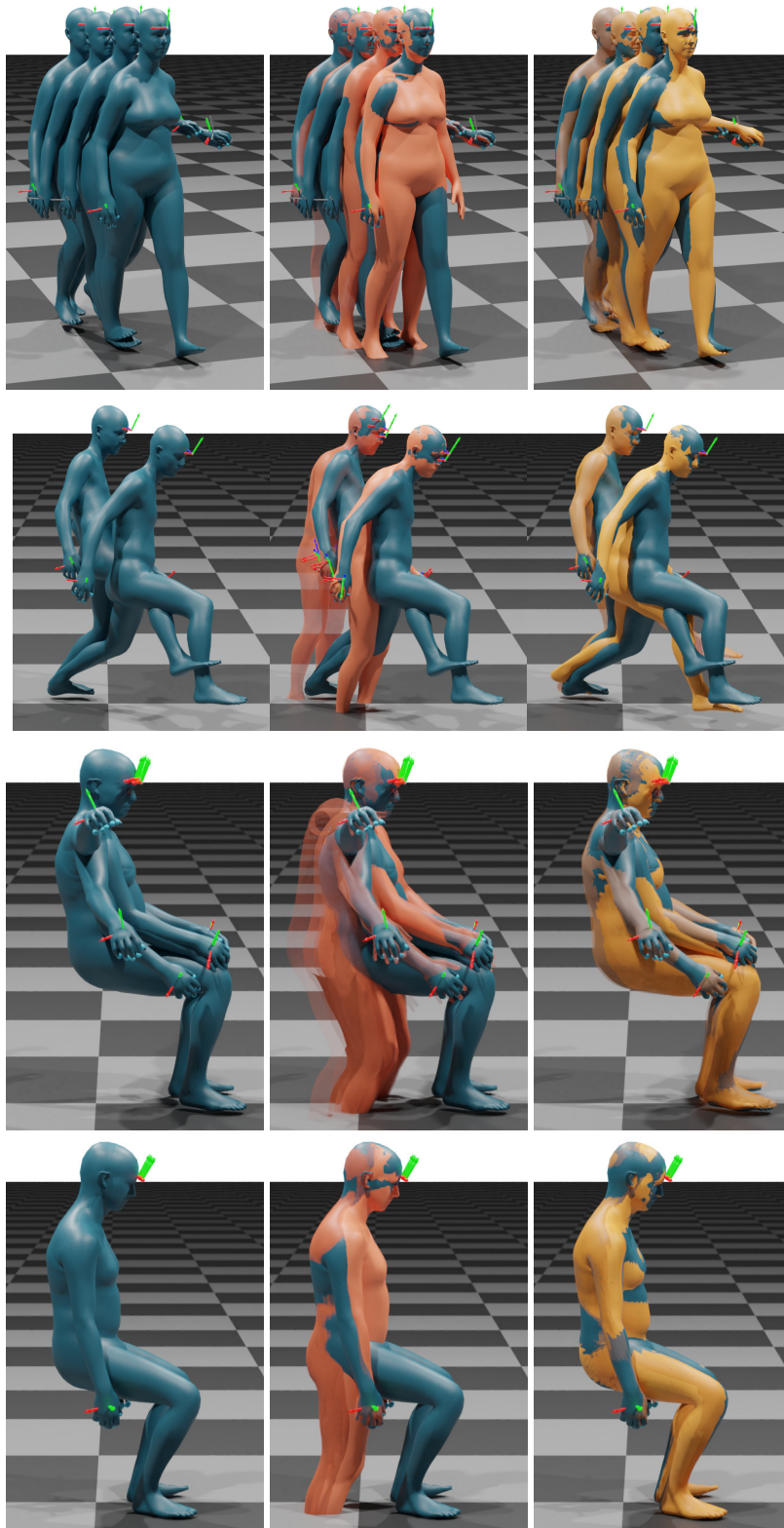


Figure 8. Comparison of the proposed learned fitter with a Levenberg-Marquardt based optimization method. From left to right: 1) Input HMD data and ground-truth mesh, 2) LM solution overlaid on the ground-truth, 3) our proposed solution overlaid on the ground-truth. While the classic approach successfully fits the input data, it still needs hand-crafted priors to prevent ground floor penetration. In contrast, our proposed fitter learns from the data to avoid solutions that violate this constraint.

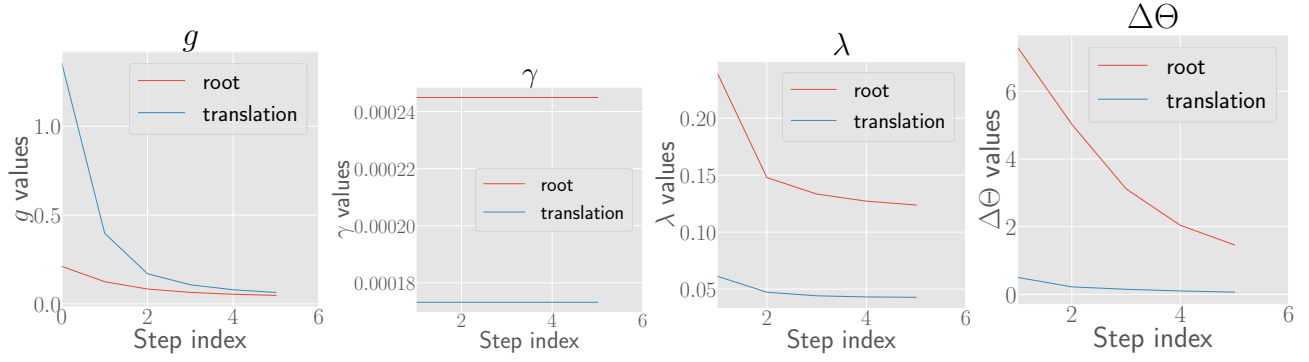


Figure 9. Average norm for (left to right) 1) $\|g_n\|_2$, 2) $\|\gamma\|_2$, 3) $\|\lambda\|_2$ and 4) $\|\Delta\Theta_n\|_2$, computed across the test set, for the root rotation and translation. The learned optimizer slows down as it approaches a minimum of the target data term.